The Astrophysical Journal, 768:17 (11pp), 2013 May 1 doi:10.1088/0004-637X/768/1/17

EVIDENCE FOR THE PHOTOSPHERIC EXCITATION OF INCOMPRESSIBLE CHROMOSPHERIC WAVES

R. J. Morton[1,2], G. Verth[1], V. Fedun[1,3], S. Shelyag[4,5], and R. Erdélyi[1]
[1] Solar Physics and Space Plasma Research Centre (SP^{2}RC), University of Sheffield, Hicks Building, Hounsfield Road, Sheffield S3 7RH, UK; richard.morton@northumbria.ac.uk
[2] Mathematics and Information Sciences, Northumbria University, Newcastle Upon Tyne NE1 8ST, UK
[3] Department of Automatic Control and Systems Engineering, University of Sheffield, Mappin Street, Sheffield S1 3JD, UK
[4] Astrophysics Research Centre, School of Mathematics and Physics, Main Physics Building, Queen's University Belfast, Belfast, County Antrim BT7 1NN, UK
[5] Monash Centre for Astrophysics and School of Mathematical Sciences, Monash University, Clayton, Victoria 3800, Australia
Received 2013 January 8; accepted 2013 March 8; published 2013 April 10

ABSTRACT

Observing the excitation mechanisms of incompressible transverse waves is vital for determining how energy propagates through the lower solar atmosphere. We aim to show the connection between convectively driven photospheric flows and incompressible chromospheric waves. The observations presented here show the propagation of incompressible motion through the quiet lower solar atmosphere, from the photosphere to the chromosphere. We determine photospheric flow vectors to search for signatures of vortex motion and compare results to photospheric flows present in convective simulations. Further, we search for the chromospheric response to vortex motions. Evidence is presented that suggests incompressible waves can be excited by the vortex motions of a strong magnetic flux concentration in the photosphere. A chromospheric counterpart to the photospheric vortex motion is also observed, presenting itself as a quasi-periodic torsional motion. Fine-scale, fibril structures that emanate from the chromospheric counterpart support transverse waves that are driven by the observed torsional motion. A new technique for obtaining details of transverse waves from time–distance diagrams is presented and the properties of transverse waves (e.g., amplitudes and periods) excited by the chromospheric torsional motion are measured.

Key words: magnetohydrodynamics (MHD) – Sun: chromosphere – Sun: photosphere – waves

Online-only material: color figure

1. INTRODUCTION

Magnetohydrodynamic (MHD) wave phenomena have now been observed to be ubiquitous throughout the solar atmosphere and are considered to be a potential mechanism for the transport of energy for the heating of the solar atmosphere and the acceleration of the solar wind (for reviews, see, e.g., Aschwanden 2005; Klimchuk 2006; Erdélyi 2006). However, no individual mechanism has yet been identified for converting a portion of the mechanical energy generated in the Sun's convection zone to heat.

Both incompressible and compressible MHD waves are widely reported throughout the solar atmosphere (for reviews, see, e.g., Banerjee et al. 2007; Zaqarashvili & Erdélyi 2009; Wang 2011; De Moortel & Nakariakov 2012) and incompressible waves in the solar wind (e.g., Tu & Marsch 1995). Recent advances in ground- and space-based solar telescopes have allowed for the detection of ubiquitous incompressible transverse waves, both in the chromosphere (De Pontieu et al. 2007; He et al. 2009a, 2009b; Okamoto & De Pontieu 2011; Antolin & Verwichte 2011; Kuridze et al. 2012; Morton et al. 2012) and in the solar corona (Tomczyk et al. 2007; Erdélyi & Taroyan 2008). However, incompressible waves are difficult to dissipate without strong gradients in Alfvén speed (e.g., resonant absorption—Ionson 1978) or some process to cause a cascade of wave energy to higher frequencies (e.g., MHD turbulence—Matthaeus et al. 1999) where they are efficiently dissipated by, e.g., cyclotron damping (McKenzie et al. 1997).

The solar magnetic field acts as a channel with the potential to distribute wave energy around the solar atmosphere. In the quiet Sun at the photospheric level, a large percentage of the magnetic flux appears to be concentrated into intense magnetic elements (spatial scales of 100–200 km) that outline the supergranule network. Some of these concentrations of magnetic flux are observed to undergo a significant expansion at the chromosphere/transition region, forming magnetic funnels that could be preferential sites for solar wind acceleration or the legs of large-scale coronal loops (Peter 2001). The remainder of the flux may form cell-spanning chromospheric structures, providing a magnetic canopy (Dowdy et al. 1986; Rutten 2006, 2007; Wedemeyer-Böhm et al. 2009). Smaller concentrations of magnetic flux also exist in the internetwork (e.g., Faurobert et al. 2001; Domínguez Cerdeña et al. 2003; Schrijver & Title 2003), potentially generating additional magnetic structure below the magnetic canopy.

The largest source of wave energy is the continually evolving sub-photospheric convection, which generates a wide spectrum of MHD fluctuations. The influence of convection on the magnetic elements is well studied at the photospheric level. Typically, the observations have focused on tracing the motion of strong, localized magnetic flux elements, referred to as magnetic bright points (MBPs) when seen in the *G*-band 4305 Å line (e.g., Title et al. 1989; Berger et al. 1995, 1998; Berger & Title 2001; Sánchez Almeida et al. 2004) or more recently in the Hα line wings (Leenaarts et al. 2006; Chitta et al. 2012). The continuous jostling of the MBPs leads to the excitation of MHD waves and oscillations, well described by the theory of MHD oscillations in magnetic flux tubes (e.g., Spruit 1982; Edwin & Roberts 1983; Erdélyi & Morton 2009; Erdélyi & Fedun 2010).

One particular aspect of convective motion that has received increased attention recently is the generation of vortices at the solar surface. Observations (Brandt et al. 1988; Bonet et al. 2008; Balmaceda et al. 2010) and advanced simulations (Moll et al. 2011; Shelyag et al. 2011b) of solar granulation have revealed that these vortex features are almost everywhere on the solar disk. Wedemeyer-Böhm & Rouppe van der Voort (2009)

and Wedemeyer-Böhm et al. (2012) have demonstrated that the vortex motion has an observable influence on the upper layers of the solar atmosphere, suggesting they may play a role in heating. Further, simulations of Fedun et al. (2011b) have demonstrated that the twisting of an open flux tube by vortices at the photospheric level leads to the generation of MHD waves, in particular incompressible (i.e., torsional Alfvén and transverse/kink) waves.

Transverse waves have recently been the subject of some controversy, with discussions on their nature, properties, and nomenclature. The properties of transverse waves in solar magnetic flux tubes are well understood (e.g., Edwin & Roberts 1982, 1983; Spruit 1982; Erdélyi & Fedun 2007), with a significant volume of research dedicated to developing realistic models, including, e.g., magnetic structuring (Verth & Erdélyi 2008; Ruderman et al. 2008), density structuring (Andries et al. 2005; Dymova & Ruderman 2005), flux tube geometry (Van Doorsselaere et al. 2004; Dymova & Ruderman 2006; Erdélyi & Morton 2009; Morton & Erdélyi 2009), multiple flux tubes (Robertson et al. 2010; Luna et al. 2010; Pascoe et al. 2011), resonant damping (Ruderman & Roberts 2002; Goossens et al. 2002, Terradas et al. 2006, 2010), and partial ionization (Soler et al. 2009a, 2009b; Zaqarashvili et al. 2011).

One of the most important properties of low-frequency transverse waves is that they are highly incompressible (Goossens et al. 2009), requiring large gradients in the Alfvén speed to damp the waves. It is this property (shared with low-frequency bulk Alfvén waves of homogeneous plasma) that means incompressible waves can pass through the lower solar atmosphere relatively undamped, making them a good candidate for accelerating solar wind. Observations of incompressible waves in the quiet chromosphere (De Pontieu et al. 2007; Morton et al. 2012), quiet corona (Tomczyk et al. 2007; Erdélyi & Taroyan 2008), and the solar wind (Tu & Marsch 1995) support this idea. Another important property that makes these waves relatively easy to observe is that the transverse wave causes a physical displacement of the axis of the flux tubes.

To assess exactly what role the incompressible MHD waves play in determining the dynamics of the solar atmosphere, one needs to combine advance models of wave propagation throughout the atmosphere (e.g., Cranmer & van Ballegooijen 2005; Cranmer et al. 2007; Matsumoto & Shibata 2010; Antolin & Shibata 2010; Fedun et al. 2011a; van Ballegooijen et al. 2011; Vigeesh et al. 2012) with observations. The observations should aim to determine how the waves are being generated and track the wave energy as it propagates through the solar atmosphere. This should reveal how much wave energy is present in each distinct region of the solar atmosphere and where the dissipation of this energy occurs. The tracking of waves through the solar atmosphere has been made a realistic possibility with the development of high spatial and temporal resolution multi-filter systems, which can observe different heights in the lower atmosphere simultaneously (e.g., Rapid Oscillations in the Solar Atmosphere (ROSA) and CRisp Imaging Spectro-Polarimeter). The potential of these observational set-ups for wave tracking is demonstrated in Vecchio et al. (2007) and Jess et al. (2012a, 2012b). Such ground-based telescopes complement the satellites, e.g., *Hinode* and *Solar Dynamics Observatory* (*SDO*), which provide detailed observations in UV/EUV.

This paper reports the observation of both chromospheric torsional Alfvén and kink waves and provides evidence that the waves are generated by photospheric vortices. The analyzed data is a high resolution, high cadence series of *G*-band, calcium K, and hydrogen α lines observed with ROSA located at the Dunn Solar Telescope, USA. The ROSA observations are supplemented with *SDO* data. Photospheric flows are determined using Local Correlation Tracking (LCT) and compared to numerical simulations of convection (Section 4). A statistical method for obtaining information on chromospheric kink waves is described based on the analysis of time–distance diagrams.

2. OBSERVATIONS AND DATA REDUCTION

The data presented here have been studied in part in Kuridze et al. (2012) and Morton et al. (2012). The data were obtained at 15:41–16:51 UT on 2010 September 29, with the Dunn Solar Telescope at Sacramento Peak, USA. A six-camera system called ROSA was employed, details of which are given in Jess et al. (2010). In brief, a $69\farcs3 \times 69\farcs1$ region of the quiet solar atmosphere, positioned close to disk center (N0.9, W6.8), was imaged with a spatial sampling of $0\farcs069$ pixel^{-1}. We note here that this is the pointing corrected from that given in Kuridze et al. 2012.

During the observations, high-order adaptive optics (Rimmele 2004) were used to correct for wave-front deformations in real time. The seeing conditions were good but variable. Some frames in each of the data series are subject to significant distortions. We exclude periods of seeing containing frames of inadequate quality.

ROSA obtained images in multiple wavelengths including *G*-band (4305.5 Å–9 Å width), Ca K (3933.7 Å) narrowband (1 Å), and Hα core (6562.8 Å) narrowband (0.25 Å) filters. The *G*-band data were sampled at 16.6 frame s^{-1}, Hα at 2.075 frame s^{-1}, and Ca K 1.66 frame s^{-1}, and the images were improved by using speckle reconstruction (Wöger et al. 2008) utilizing a 16–1 ratio. The cadence of the reconstructed *G*-band, Hα, and Ca K time series are 0.96 s, 7.7 s and 9.6 s, respectively. To ensure accurate co-alignment in all bandpasses, the broadband times series were Fourier co-registered and de-stretched (Jess et al. 2007).

Images from the *SDO* Atmospheric Imaging Assembly (AIA) are also presented to provide context for the state of the upper atmosphere above the ROSA field of view. The images from *SDO* are processed with *aia_prep* and have a spatial resolution of $0\farcs6$ pixel^{-1}.

3. THE MAGNETIC STRUCTURE

The region of the Sun observed by ROSA is a typical quiet-Sun area. The focus of the investigation will be on a sub-region of the ROSA field of view that contains a feature of particular interest. Images of this sub-region are shown in Figure 1. In the *G*-band images, a number of MBPs are clearly identifiable. The bright points are a good proxy for strong concentrations of magnetic flux; however, strong magnetic flux can still be present without an associated MBP (Berger & Title 2001). Specific conditions appear to be needed for an MBP to appear in the *G* band (e.g., Carlsson et al. 2004; Ishikawa et al. 2007). On viewing the movie of the *G*-band time series, the MBPs are seen to be pushed and jostled by the convective motions of the granules, merging and splitting, and appearing and disappearing from the bandpass.

The Ca K images (Figure 1(b)) also show bright points, displaying a close mapping to the MBPs seen in *G* band. This suggests the Ca K bright points are the chromospheric counterpart to the *G*-band MBPs. However, the Ca K bright points are more diffuse, possibly due to expansion of the magnetic flux with

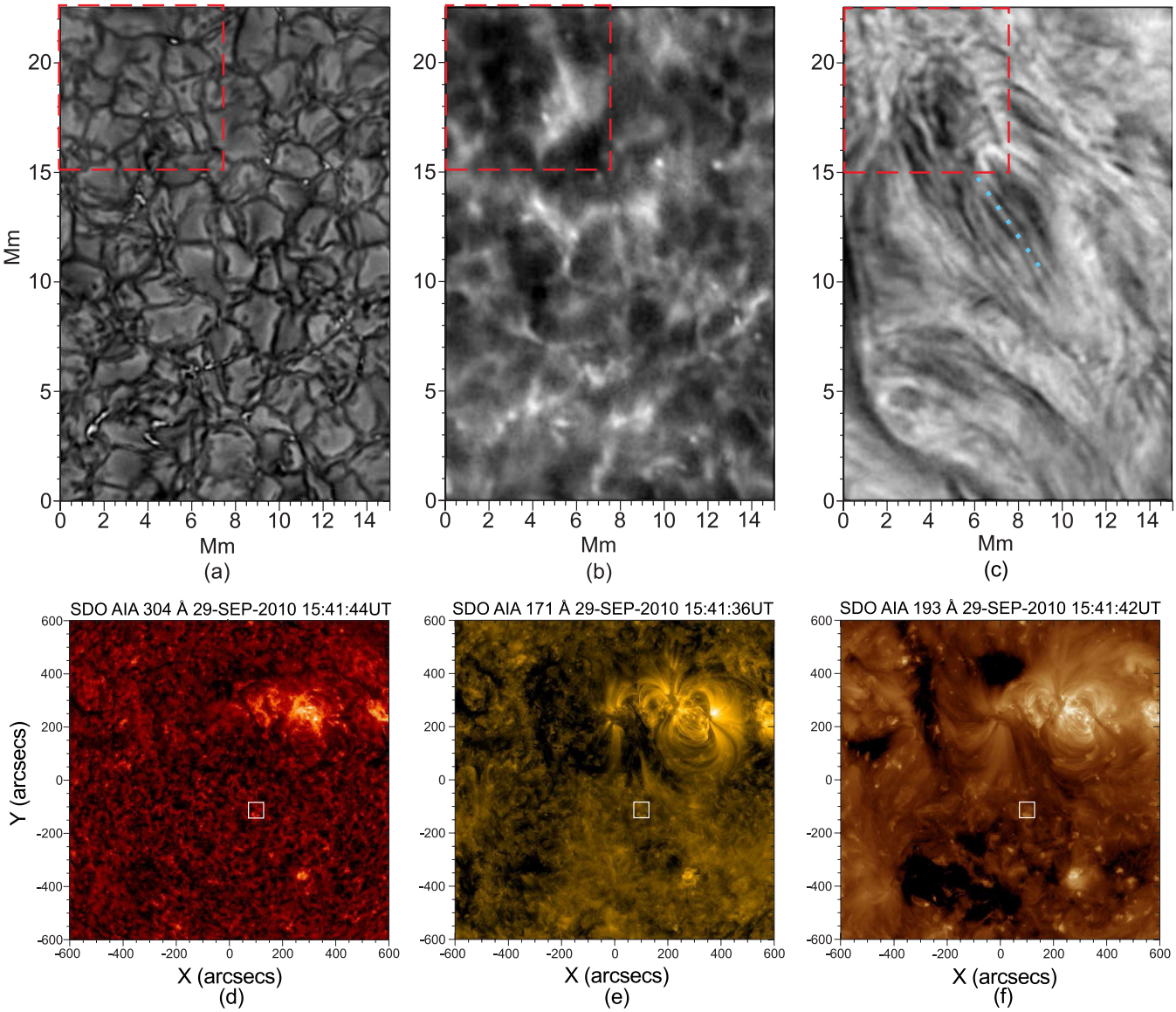

Figure 1. Region of the quiet solar atmosphere as observed by ROSA. (a) *G*-band image showing a 15 × 23 Mm^2 sub-region of the ROSA field of view. Collections of magnetic bright points are clearly visible in the intergranule lanes. (b) Ca K image of the lower chromosphere. (c) Hα core image of the mid to upper chromosphere. The existence of fine-scale structuring in the bandpass is evident, with both spicules/mottles and cell-spanning fibrils identifiable. The blue dots show the path along which perpendicular cross-cuts were taken; see Section 5 for further details. The bottom row displays images of the upper solar atmosphere observed by *SDO*/AIA. The panels show (d) 304 Å, (e) 171 Å, and (f) 193 Å filters. The axis show solar coordinates. The white boxes highlight the region which ROSA observed.

(A color version of this figure is available in the online journal.)

height and partially due to the properties of the filter. The bright points are also more persistent than the *G*-band MBPs, and hence show a different morphology. The images also contain acoustic grains and reversed granulation, which have been identified previously. These features (possibly including the diffuse MBP nature) are present due to the large width of the filter bandpass used for these observations, meaning that the Ca K images here have contributions from both photospheric and chromospheric sources (for a detailed explanation, see Leenaarts et al. 2006). Selecting a sufficiently narrow filter to image the Ca K line center can avoid photospheric contamination and allow mainly chromospheric contributions (see, e.g., Cauzzi et al. 2008; Reardon et al. 2009; Pietarila et al. 2009).

In the Hα core bandpass (Figure 1(c)), few signatures of the MBPs are visible. The region is covered with fine-scale structure, such as elongated, cell-spanning fibrils and a few shorter mottles (jet-like structures). Due to the narrow width of the filter, the Hα core images show the "true," magnetically dominated (low-β) chromosphere (Rutten 2006, 2007). The observed features, i.e., the fibrils and mottles, are thought to highlight the chromospheric magnetic field, with the structures likely to be density enhancements along individual magnetic field lines (this is supported by recent modeling of Hα line formation by Leenaarts et al. 2012).

In the following section, we pay particular attention to the area highlighted by the dashed box in Figure 1. A number of fibrils and mottles can be seen to emanate from this region. At the photospheric level, the *G*-band images reveal that a number of MBPs appear and disappear. The counterpart Ca K bright points remain present, although some of the brighter elements fade and brighten with time. These underlying features lead us to suggest the highlighted Hα region is the chromospheric section of a magnetic flux concentration, associated with an MBP, that has undergone significant expansion from the photosphere.

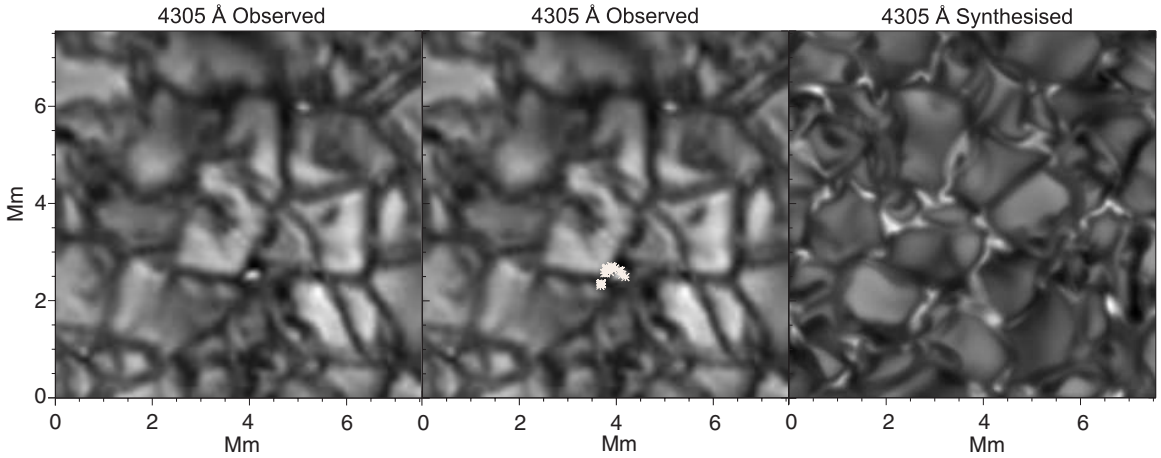

Figure 2. Left panel displays the *G*-band region enclosed in the red box in Figure 1. Middle panel: the motion of an MBP flow derived with a point and click method is highlighted by the overplotted stars. The motion is from left to right. The right image is the synthesized *G* band from the MURaM code.

The diameters of the observed MBPs are ∼100–200 km, while the Hα feature has a diameter of ∼3000 km. The described magnetic structure is thought to be common in the quiet solar atmosphere (e.g., Dowdy et al. 1986; Peter 2001) and is also revealed in observations of chromospheric swirls by Wedemeyer-Böhm & Rouppe van der Voort (2009) and Wedemeyer-Böhm et al. (2012).

The magnetic structure above the chromosphere is much harder to determine. Figures 1(d)–(f) display images from *SDO*/AIA in the 304 Å, 171 Å, and 193 Å bandpasses. A nearby active region is visible in the upper right hand corner of each image; however, it can be seen that the ROSA field of view is far from the active region in an area of quiet Sun.

4. FLUX TUBE DYNAMICS

Now, our attention is focused on the dynamical behavior of the unique region identified in the previous section (dashed box—Figure 1). To provide insight into the horizontal motions of the magnetic elements, we exploit LCT. This technique was originally introduced into solar physics to track large-scale (spatial and temporal) photospheric flows, e.g., November & Simon (1988), and the technique has been developed further for use on magnetograms by incorporating the induction equation (e.g., DAVE—Schuck 2006).

We developed an LCT algorithm based on the routine *tr_get_disp.pro* (developed by T. Tarbell) available in the SSW TRACE software tree. A recent version of this routine first apodizes a set of images using a Hanning function, then computes the cross-correlation between the images. The position of the maximum of the cross-correlation corresponds to the integer pixel shifts between the images. A local region centered on the maximum is then fitted with a quadratic polynomial regression equation to locate the maximum with sub-pixel accuracy, hence providing sub-pixel accuracy on the shifts.

The routine was tested on sample data, which consists of hundreds of different images taken from the ROSA data series. The images were shifted using the routine *shift_image.pro* (available in the general SSW software tree). Taking averages over large numbers of images, we find that shifts as small as 0.03 pixels can be resolved to within ±0.005 pixels. The accuracy of the LCT improves with increasing shift size. There appears to be potential for great accuracy when calculating small shift values statistically; however, a more rigorous test of *tr_get_disp*'s ability to resolve shifts is needed.

From the derived shifts, we are able to determine the horizontal photospheric flow, U_h. Further, we can calculate the divergence of the velocity, $\nabla \cdot U_h$, and the photospheric vorticity, $\nabla \times U_h$.

4.1. LCT on G-band Data

The *G*-band data series has a very high cadence at 0.96 s. However, the previously reported values for photospheric flows are 1–2 km s^{-1}, hence the expected shift between each frame is <0.03 pixels. To improve accuracy, every eighth frame is then selected from the *G*-band series, increasing the cadence to 7.68 s and expected shifts to >0.08 pixels (0.5 km s^{-1}). Further, a sonic filter is applied to the data to suppress the influence of *p*-modes and stochastic variations in intensity. The data is then re-sampled using linear interpolation to achieve a pixel size of 25×25 km^2.

The LCT is performed on frames chosen from the first 60 frames because the seeing during this period is relatively stable. For each data set that we apply LCT to, the LCT is preformed on many sub-regions of the overall image, with window sizes determined by the dominant features at that wavelength. A window size of 40×40 pixel^2 (1×1 Mm^2) is used such that features on the order of the granulation will contribute to the cross-correlation. This, along with the apodization of the window, will reduce the effect of large intensity gradients on resolving shifts.

The 7.5×7.5 Mm^2 boxed region in Figure 1(a) is selected (close-up of this region is shown in Figure 2, left panel) and subject to the LCT algorithm. The photospheric flow is calculated over a 30 frame average, revealing long-lived flow patterns.

The magnitude of the photospheric velocities are shown in Figure 3. A histogram plot of the velocity distribution (Figure 3) is in line with results from MBP tracking, e.g., Keys et al. (2011) and Chitta et al. (2012), and from long-term flow measurements, e.g., November & Simon (1988) and Berger et al. (1998). The velocity vectors and divergence are also shown in Figure 3. The directions of the velocity vectors results are consistent with the flow direction as seen by a visual inspection of the *G*-band movie. Evidence for vortices are present, with the velocity vectors marking out curved paths or arcs thought to be demonstrating the vortex behavior. This is verified by calculating the vorticity from the horizontal velocity, which demonstrates that vorticity is present across the photospheric

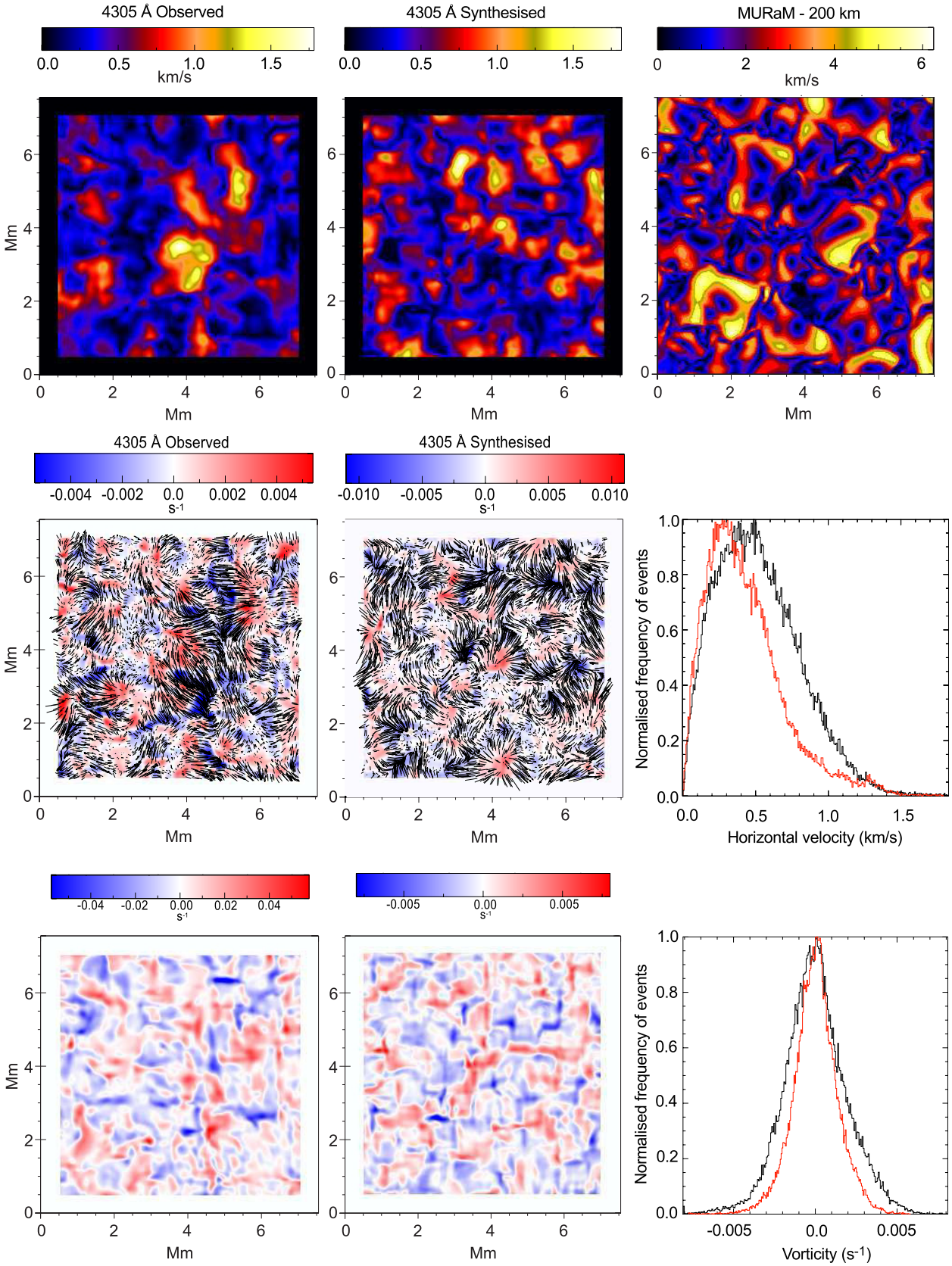

Figure 3. Left: the top row shows the magnitudes of velocities of photospheric flows as determined from the observed *G* band, middle: the synthesized *G* band, right: and the MURaM code at a geometric height of 200 km above the continuum formation level. The velocities are averaged over 30 frames (∼230 s). The middle row displays velocity vectors and divergence of photospheric flows. The arrows display the averaged velocity vectors determined with LCT from the observed (left) and simulated (middle) *G* band. A histogram (right) showing the distribution of the horizontal velocity for the observed (red) and the simulated (black) data. The bottom row displays vorticity (s^{-1}) calculated from the horizontal photospheric flows. The panels displays the averaged vorticity from the observed (left) and simulated (middle) *G* band. A histogram (right) showing the distribution of the vorticity for the observed (red) and the simulated (black) data.

region (Figure 3—bottom row, left panel). A histogram of vorticity values is given in Figure 3 and the values obtained here are in agreement with previous observational measurements (e.g., Brandt et al. 1988; Vargas Domínguez et al. 2011).

In addition, the motion of an individual MBP is tracked over 20 frames using a crude (but efficient) point and click method. The MBP selected lies directly under the chromospheric feature, which suggests it is the photospheric counterpart. The tracking of the individual bright point reveals the MBP follows an arc-shaped path across the photosphere, demonstrating the MBP is in the presence of a photospheric vortex. This is confirmed as the MBP is also seen to lie in a region of strong, negative vorticity in Figure 3.

4.2. LCT on Simulated G-band Data

To validate the results of the LCT technique, we performed tests on a numerically simulated *G*-band image sequence. The synthetic data were produced using radiative diagnostics of the three-dimensional numerical model of magnetized lower solar atmosphere (i.e., convection zone and photosphere) generated by the MURaM radiative MHD code (Vögler et al. 2005). The chosen domain size is $12 \times 12 \times 1.4\,\mathrm{Mm}^3$ in the horizontal and vertical directions, respectively, and the horizontal resolution is 25 km. The detailed *G*-band radiative diagnostics was carried out using the radiative transport code, designed for computationally efficient wide-band filter calculations (see Jess et al. 2012b for more details). We have generated 800 *G*-band images of solar granulation with the average vertical magnetic flux of 200 G (the value of the magnetic field strength is consistent with recent observations, e.g., Orozco Suárez & Bellot Rubio 2012). The time cadence for the image sequence is about 2 s and not constant due to the variation of the time step in the numerical simulation.

To provide a direct comparison with the observational analysis described in the previous section, the resolution of the simulated data is reduced to 50 km, using every fourth frame to achieve a similar cadence. We apply the sonic filter and resample using linear interpolation to 25 km. The LCT results are averaged, again, over 30 frames. The results of LCT on the simulated *G*-band image sequence demonstrate qualitatively similar plasma flow patterns in both the granular and intergranular regions to the observed data (Figure 3). The results from the simulated data show slightly greater values of divergence and vorticity. The absolute values of velocity and vorticity in the simulated data are plotted in a histogram (Figure 3) for direct comparison between the observed and synthesized *G*-band images. The distributions can be seen to be comparable although slight differences exist between the observed and simulated values. This can be attributed to the fact that the observed and simulated regions are inherently different regions, with an unknown quantity of magnetic flux in the observed region. Some of the differences may also lie in the quality of the observed data. A measure of the difference in quality is the root-mean-squared contrast. The synthesized *G*-band images have a mean rms of 0.17 ± 0.003, while the observed *G*-band images have a much lower mean rms of 0.11 ± 0.02 and much greater variation in rms between frames.

The flow speeds in the simulations have also been measured at the geometrical height of approximately 200 km above the continuum formation level. They show the presence flow features similar to those detected by LCT applied to the simulated *G*-band images (Figure 3). However, due to measurement of the flow speeds at the constant geometrical height instead of at optical depth corresponding to the *G*-band radiation formation, only a qualitative comparison of these speeds with the speeds obtained by LCT is valid and possible.

The simulations are known to be replete with vortex motions. The agreement seen between LCT results performed on the observed and simulated data gives us confidence that the photosphere also contains numerous vortex structures. Torsional Alfvén waves have been shown to be excited at the photospheric level in a number of numerical simulations. They are excited in magnetic photospheric vortex structures by random motions, such as granular flows (see, for example, numerical simulations of photospheric magnetoconvection, e.g., van Ballegooijen et al. 2011; Kitiashvili et al. 2011; Shelyag et al. 2011a, 2012a, 2012b; Moll et al. 2012), and by synthetic photospheric torsional (vortex-type) drivers (e.g., Fedun et al. 2011a, 2011c; Vigeesh et al. 2012) in the idealized simulations of solar magnetic flux tubes.

We note that the magnetic vortex structures significantly differ in their nature and dynamics from the non-magnetic vortices (see, e.g., Stein & Nordlund 1998; Kitiashvili et al. 2012). They, and the torsional Alfvén waves they produce, generate large amounts of Poynting flux (see, e.g., Fedun et al. 2011b, Shelyag et al. 2012a, 2012b). As has been shown by Wedemeyer-Böhm et al. (2012), the magnetic vortex structures expand from the photospheric level into the corona. They are suggested channels for electromagnetic energy to tunnel into the higher layers of the solar atmosphere and, therefore, such structures are considered as potential channels of energy transport for coronal heating.

4.3. LCT on Hα Data

On inspecting the Hα movie, a torsional (or rotational) motion is observable in the area highlighted with the dashed box in Figure 1(c). A chromospheric response to photospheric vortices has already been observed in high-resolution observations of the lower chromosphere (Wedemeyer-Böhm & Rouppe van der Voort 2009; Wedemeyer-Böhm et al. 2012). So far, the reported chromospheric swirl events appear to demonstrate rotation in *one* direction only. Here, the Hα region appears to first rotate in one direction and then rotate in opposite direction quasi-periodically. Such behavior has been observed in the intergranular vortices in realistic simulations of magnetoconvection (Shelyag et al. 2011b, 2012a), as well as in the idealized simulations of flux tubes in the quiet Sun (Fedun et al. 2011c). This would suggest the presence of torsional Alfvén waves, which have also been identified previously in chromospheric features situated above MBPs (Jess et al. 2009).

To demonstrate this behavior, LCT is applied to the Hα data. Before performing LCT, the unsharp-mask (USM) technique is applied to the full field of view and the mask is subtracted. The mask is created using a box-car average of width 20 pixels. This technique has two benefits: (1) the removal of large spatial-scale intensity perturbations which could influence results; (2) an increased contrast between chromospheric features and the background. The intensity perturbations (Morton et al. 2012) are removed from the time series because they are coherent over a large spatial scale. Further, an atrous spatial filtering algorithm (e.g., Starck & Murtagh 2002) is applied to each frame. The highest frequency component from the spatial filtering contains mainly noise, which is then subtracted to improve the signal to noise in each image.

The torsional motion appears quasi-periodic with an apparent period between 120 and 180 s; hence, the LCT is averaged over sets of nine consecutive frames. Note that the period range given is based on the apparent rate at which the motion

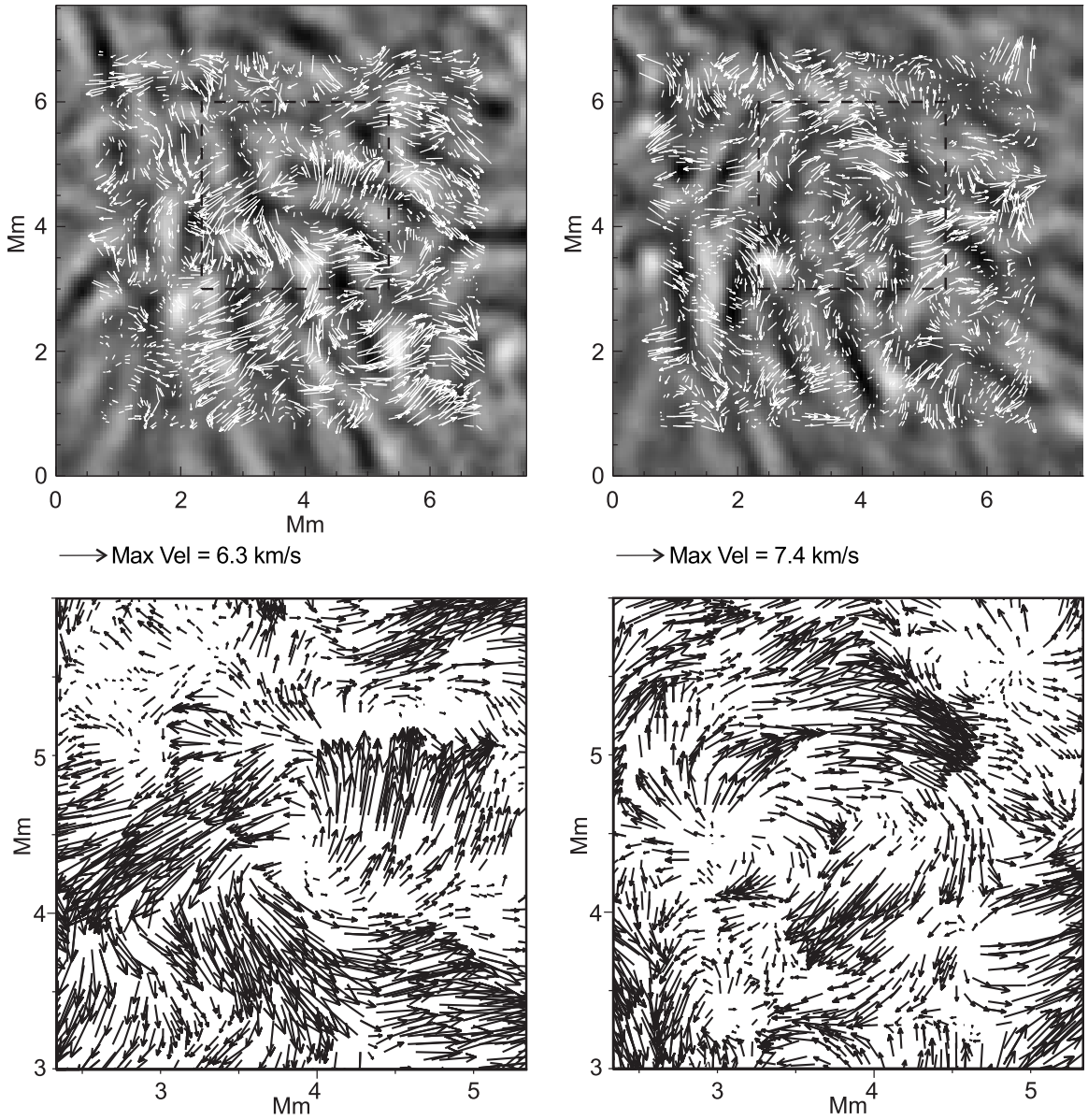

Figure 4. Chromospheric response to photospheric vortices. Torsional motion is observed in Hα and demonstrated by applying LCT to frames between $t = 207$–277 s (left) and $t = 610$–690 s (right). The torsional motion is centered approximately on the point located at (3.8, 4.5) Mm. The vectors are overplotted on the unsharp masked and atrous filtered Hα data at $t = 200$ s (left) and $t = 600$ s (right). The region shown corresponds to the dashed box in Figure 1(c). The bottom row displays enlarged versions of the regions centered on (3.8, 4.5) Mm (as marked by the boxes). The density of vectors has also been increased by a factor of two and a half.

appears to change its direction of rotation. The time series shows the rotation change directions a number of times over its duration. This is calculated by eye from viewing the Hα time series and we do not consider it a rigorous measurement of the period. The velocity vector plots in Figure 4 confirm the visual impression of torsional motion. The first vector plot is averaged over the frames in the range 207–277 s and the second vector plot is averaged over 610–690 s. These time ranges are used as they correspond to the times when the torsional motion is most evident. The torsional motion is centered on the region around (3.8, 4.5) Mm in the plots and a zoom of this region (Figure 4—bottom row) reveals the signature of the torsional motion. The maximum values of the velocity amplitude of the torsional motion are $\sim$7 km s^{-1} with an average and standard deviation of 1.8 ± 1.4 km s^{-1}. These values are essentially the time-averaged velocity amplitudes, while the peak amplitudes are likely greater as the peak value is a factor of $\sqrt{2}$ greater than the time-averaged amplitude.

5. TRANSVERSE WAVES

The focus of this work is now shifted to the fine-scale structure that originates in the previously identified Hα region. The fine-scale structure we are interested in are the dark, absorption features, which are mainly elongated, inclined fibrils and a few mottles (nearly vertical structures thought to be similar to spicules). On inspecting the movie of Hα, the fine-scale structure can be identified to exhibit transverse motion. The fibrils are rooted in the region where the torsional motion is observed and the torsional motion shakes the fibrils footpoints side to side, which drives the transverse waves. In this section, we study the transverse waves supported by these structures and demonstrate new techniques for obtaining information about the waves.

To model these transverse waves, the assumption is made that the waves are propagating along an overdense, magnetic flux tube embedded in an ambient plasma environment. The speed at which these waves propagate is known as the kink

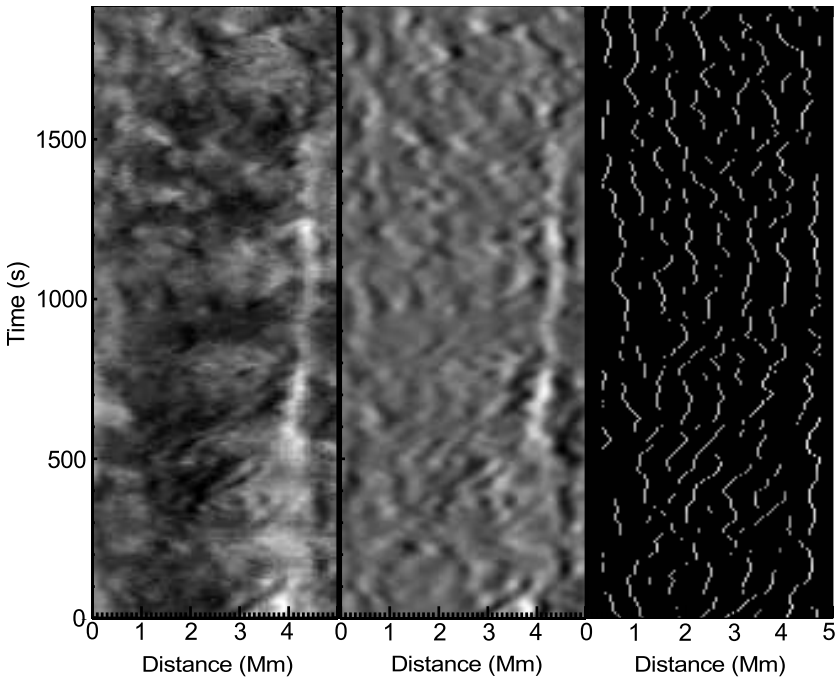

Figure 5. Overview of the technique for identifying transverse waves. The left panel shows time–distance plot of a cross-cut taken perpendicular to the fibrils (i.e., perpendicular to the dotted blue line in Figure 1(c)). The middle panel is the same cross-cut that has been subject to unsharp mask and with the high-frequency component removed. The right panel displays the fibril paths obtained from the time–distance plot in the middle panel. The lines highlight the dark features.

speed, which is defined as

$$c_k = \sqrt{\frac{\rho_i v_{Ai}^2 + \rho_e v_{Ae}^2}{\rho_i + \rho_e}}, \quad (1)$$

where ρ is the density, $v_A = B^2/(\rho\mu_0)$ is the Alfvén speed, B is the magnetic field, and μ_0 is the magnetic permeability. Here, we follow convention, labeling internal and ambient plasma parameters with subscripts i and e, respectively.

The first step in the analysis of the observed transverse waves is to apply the USM procedure to the Hα images. The orientation of the fine-scale structure is determined (see dotted line overplotted on the Hα image; Figure 1(c)) and a series of 42 cross-cuts, separated by 2 pixels, are placed perpendicular to their axis. From the cross-cuts, time–distance plots are created, an example of which is shown in Figure 5. The time–distance plots clearly reveal the transverse motions of the fibril structures. Next, to reduce the background noise, an atrous filtering algorithm is applied to the time–distance plots and the highest frequency component is subtracted.

The individual dark fibrils in each cross-cut are then located in the following manner. Cross-sectional flux profiles of fibrils have an almost Gaussian shape, with the minimum value of intensity at the center of the fibril cross-section. For each time slice, the pixels with the minimum intensity in a localized region are located. A gradient threshold is then applied allowing for isolated fibrils to be located. The gradient of the neighboring five points on either side of the minimum value pixel is calculated and has to be larger than the threshold value for the minimum point to be selected. Should two fibrils approach each other or begin to cross, the gradient becomes shallower around the minima. Optimization of the threshold level allows for a significant number of isolated fibrils to be identified (Figure 5(c)), with the fibril paths in time being traced out. This method only locates the center of the structure to within one pixel and hence has an error of $\pm$50 km on each point.

For each fibril path identified at this stage, we then select only the paths that obey certain conditions: (1) the path has to be longer than 5 pixels; (2) the maximum time separation between neighboring points in the thread has to be less than 4 pixels (30 s), the "missing" pixels are then recorded as having the same spatial position as that of the first of the time-separated neighbors; (3) points neighboring in time cannot be separated spatially by more than 4 pixels (200 km). This last condition would limit any measured velocity amplitudes to $<$26 km s^{-1}.

Once we have selected the fibril paths, the results are then fitted with a Levenberg–Marquardt nonlinear fitting algorithm (mpfit.pro—Markwardt 2009). A function of the form

$$F(t) = G(t) + A\sin(\omega t - \phi) \quad (2)$$

is used to fit the oscillations. Here, $G(t)$ is a linear function, A is the displacement amplitude of the oscillation, ω is the frequency, and ϕ is the phase of the oscillation. The fitting algorithm is supplied with the errors on each data point, where it is assumed the given error is the 1σ uncertainty. The fitting routine also calculates the 1σ error to each fit parameter. The fitted results are kept if the threads are longer than $3 \times 2\pi/4\omega$ and the errors on the fitted parameters are smaller than the magnitude of the parameter values. Transverse velocity amplitudes for the waves can be obtained from the fit using the relation $v_\perp = \omega A$ and errors in the velocity amplitude are calculated by summing in quadrature.

Over the 42 cross-cuts a total of 1100 oscillations are measured. A histogram of the periods, transverse amplitudes, and velocity amplitudes are given in Figure 6. A Gaussian fit to the distributions gives means and standard deviations of $P = 94 \pm 61$ s, $A = 71 \pm 37$ km, and $v_\perp = 4.5 \pm 1.8$ km s^{-1}. It is also interesting to plot period versus displacement amplitude (Figure 6—bottom row, left panel). It is apparent that there is a direct relationship between the transverse displacement amplitude and period. We perform a weighted linear fit to the

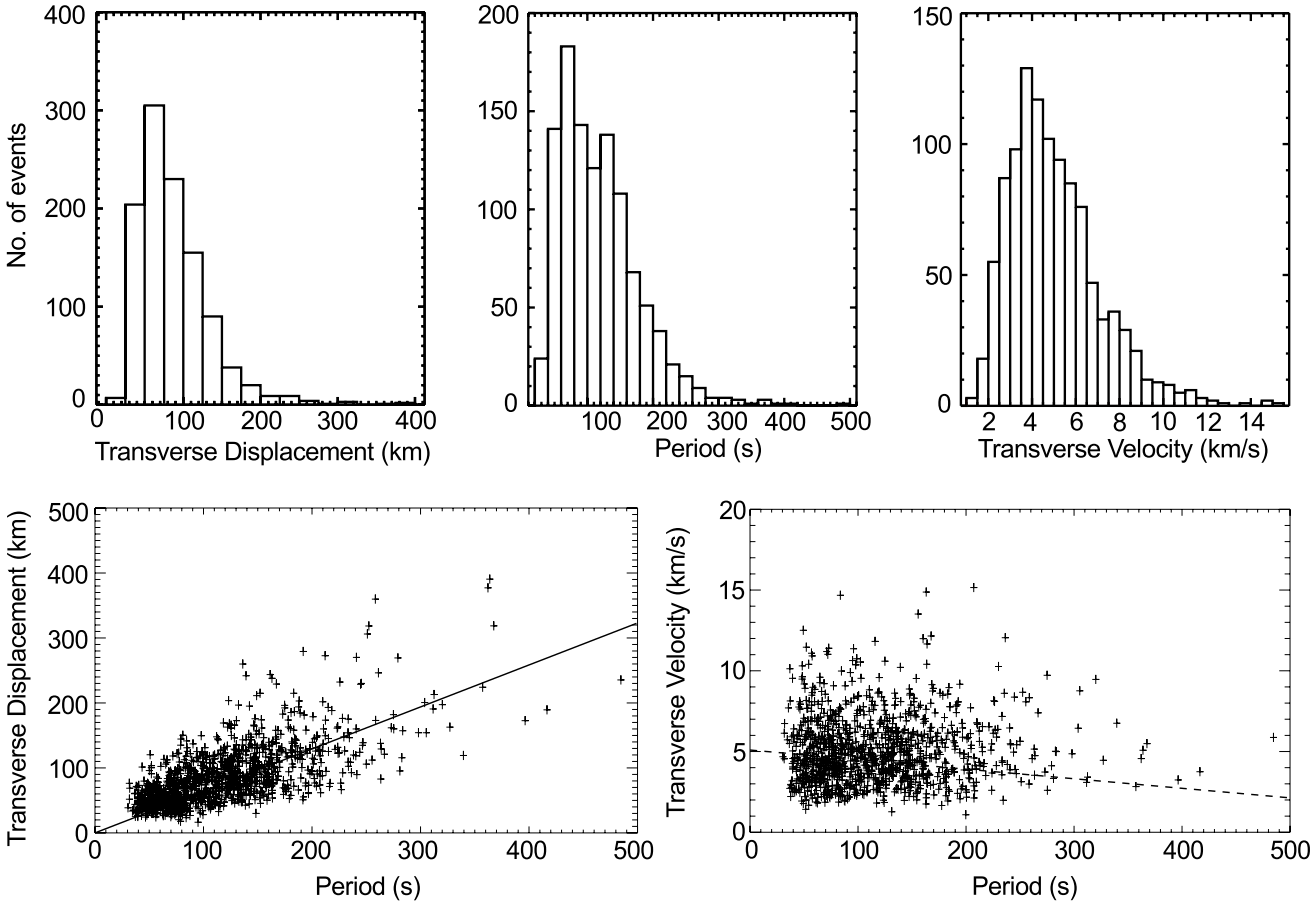

Figure 6. Top: histograms of measured properties of transverse motions for chromospheric fine structure originating in the region displaying torsional motion. The histograms show, from left to right, the period, transverse displacement amplitude, and transverse velocity amplitude. The mean and standard deviations are $P = 94 \pm 61$ s, $A = 71 \pm 37$ km, and $v_\perp = 4.5 \pm 1.8$ km s^{-1}. Bottom: measured properties of the transverse waves. Left: period vs. displacement amplitude. The solid line is a weighted fit to data points that gives a velocity amplitude of ∼4.5 km s^{-1}. Right: period vs. velocity amplitude. The dashed line is the weighted linear fit to the data points.

data points, calculated with the Levenberg–Marquardt algorithm with the constraint the line passes through (0, 0). The result is overplotted and the derived velocity amplitude from the trend is ∼4.2 km s^{-1}, in agreement with the mean value.

In Figure 6 (bottom row, right panel), the velocity amplitude as a function of period is shown. Qualitatively, the velocity amplitude appears relatively constant as a function of period; however, a weighted linear fit to the data points suggest the velocity amplitude decreases with period. This implies that the energy, which is proportional to the square of the velocity, contained within this frequency range of waves (2–30 mHz) is approximately constant as a function of period. It is worth noting that the estimates of the temporal power spectra of the horizontal velocity of the photosphere by Matsumoto & Kitai (2010) using the *G*-band filter of *Hinode*/Solar Optical Telescope showed a change of trend in the log–log gradients of Fourier power versus frequency at 4.7 mHz (approximately 213 s period). For frequencies less than 4.7 mHz, they found an $f^{-0.6}$ relationship and for frequencies greater than 4.7 mHz it was $f^{-2.4}$. The derived photospheric power spectra, found by the method of LCT, were taken as a proxy for the actual photospheric driver of transverse waves for a numerical simulation by Matsumoto & Shibata (2010; in their case the $m = 0$ torsional Alfvén wave and not the $m = 1$ kink waves we observe here). A number of questions now arise, in comparing our measurements of transverse chromospheric velocity amplitude versus period measurements in chromospheric fibrils with the photospheric power spectra of Matsumoto & Kitai (2010). First, our results suggest that Matsumoto & Shibata (2010) may have used the incorrect input power spectra, i.e., we see no evidence of wave energy decreasing with decrease in period. This is particularly relevant for wave heating since mechanisms such as resonant absorption, phase mixing, and ion-neutral damping are all more efficient at higher frequencies. On the other hand, if the photospheric power spectra obtained by Matsumoto & Kitai (2010) are a reasonable proxy for the driver of transverse waves, the output is notably different at chromospheric heights and must be explained by further study.

We should note that all fits calculated here are under the assumption that the error in the period can be neglected over the error in the transverse displacement and velocity amplitudes. This may be justified as the mean error on the period, transverse displacement, and velocity amplitudes are 8%, 21%, and 23%, respectively.

6. DISCUSSION AND CONCLUSIONS

Tracking wave propagation through the lower layers of the solar atmosphere is an important step in being able to assess the viability of the various suggested mechanisms for atmospheric heating and solar wind acceleration. In Section 4, we present observational evidence that photospheric vortices occur in the regions of strong magnetic flux concentrations. This is found to be in good agreement with the predictions of advanced models of solar magnetoconvection. Further, we provide evidence that

demonstrates photospheric vortices can excite torsional motions in the chromosphere. This is supported by previous results from various numerical simulations (e.g., van Ballegooijen et al. 2011; Kitiashvili et al. 2011; Shelyag et al. 2011a, 2012a, 2012b; Fedun et al. 2011a, 2011c; Moll et al. 2012; Vigeesh et al. 2012) and previous observations (e.g., Wedemeyer-Böhm et al. 2012). The observation of vortex and torsional motions is achieved by exploiting LCT to track the motions of both photospheric and chromospheric features and identifying the signatures in the resulting velocity vector plots. The chromospheric torsional motion appears periodic here (unlike the unidirectional motion identified in swirl events, e.g., Wedemeyer-Böhm & Rouppe van der Voort 2009), although we cannot resolve the periodic behavior explicitly. The vector plots demonstrate that the region rotates one way and, at a later time, in the opposite direction. A better way to obtain details on torsional waves may be to exploit spectroscopic observations (e.g., Jess et al. 2009).

Further, the torsional motion is observed to excite transverse waves in the chromospheric fine structure whose footpoints are rooted in the region. The fine structure takes the form of elongated absorption features that are fibrils and a few shorter features, possibly mottles. The transverse velocity amplitudes of the transverse waves are comparable to the velocity amplitudes obtained from the averaging of the torsional motion. The observations imply that the transverse waves are driven by torsional motion, which in turn is driven by photospheric vortices. The transfer of energy from photospheric vortices to Alfvén waves and chromospheric transverse waves has been demonstrated in numerical simulations of the lower solar atmosphere (e.g., Fedun et al. 2011b).

The measured wave properties also reveal interesting information about the chromospheric waves. In particular, the measured velocity amplitudes (Figure 6) suggest that waves with periods in the range 50–500 s have similar power. However, the results presented here are restricted to incompressible waves confined in one particular structure in the chromosphere. A more in-depth study taking into account numerous chromospheric structures is required before more definite conclusions on this issue can be drawn.

Finally, we highlight here that our results have some limitations. The limitations are related to the inability to resolve small amplitude ($\lesssim$25 km) transverse waves due to spatial resolution. The demonstrated relationship between displacement amplitude and period (Figure 5) implies that spatial resolution also limits the ability to detect short-period waves ($\lesssim$30 s). On the other end of the scale, the known lifetimes of the chromospheric structures (i.e., 3–5 minutes) also limits the observations of longer period waves ($>$200 s). This is reflected in the low number of observations of wave with longer periods. Some of these limitations may be overcome if more advanced techniques are employed for wave tracking, e.g., calculating sub-pixel displacements could reveal smaller amplitude wave phenomena.

The authors thank D. B. Jess, M. Mathioudakis, and A. Hillier for a number of helpful discussions. Observations were obtained at the National Solar Observatory, operated by the Association of Universities for Research in Astronomy, Inc. (AURA) under agreement with the National Science Foundation. We thank the technical staff at DST for their help and support during the observations. This work is supported by the UK Science and Technology Facilities Council (STFC). R.M. is grateful to Northumbria University for the award of an Anniversary Fellowship and to the Royal Astronomical Society (RAS) for the award of an RAS travel grant. G.V. is grateful to the Leverhulme Trust for the award of a fellowship. S.S. research is supported by the Australian Research Council Future Fellowship. R.E. acknowledges M. Kéray for patient encouragement and is also grateful to NSF, Hungary (OTKA, Ref. No. K83133).

REFERENCES

Andries, J., Arregui, I., & Goossens, M. 2005, ApJL, 624, L57
Antolin, P., & Shibata, K. 2010, ApJ, 712, 494
Antolin, P., & Verwichte, E. 2011, ApJ, 736, 121
Aschwanden, M. J. 2005, Physics of the Solar Corona. An Introduction with Problems and Solutions (2nd ed.; Chichester: Praxis Publ. Ltd.)
Balmaceda, L., Vargas Domínguez, S., Palacios, J., Cabello, I., & Domingo, V. 2010, A&A, 513, L6
Banerjee, D., Erdélyi, R., Oliver, R., & O'Shea, E. 2007, SoPh, 246, 3
Berger, T. E., Loefdahl, M. G., Shine, R. S., & Title, A. M. 1998, ApJ, 495, 973
Berger, T. E., Schrijver, C. J., Shine, R. A., et al. 1995, ApJ, 454, 531
Berger, T. E., & Title, A. M. 2001, ApJ, 553, 449
Bonet, J. A., Márquez, I., Sánchez Almeida, J., Cabello, I., & Domingo, V. 2008, ApJL, 687, L131
Brandt, P. N., Scharmer, G. B., Ferguson, S., Shine, R. A., & Tarbell, T. D. 1988, Natur, 335, 238
Carlsson, M., Stein, R. F., Nordlund, Å., & Scharmer, G. B. 2004, ApJL, 610, L137
Cauzzi, G., Reardon, K. P., Uitenbroek, H., et al. 2008, A&A, 480, 515
Chitta, L. P., van Ballegooijen, A. A., Rouppe van der Voort, L., DeLuca, E. E., & Kariyappa, R. 2012, ApJ, 752, 48
Cranmer, S. R., & van Ballegooijen, A. A. 2005, ApJS, 156, 265
Cranmer, S. R., van Ballegooijen, A. A., & Edgar, R. J. 2007, ApJS, 171, 520
De Moortel, I., & Nakariakov, V. M. 2012, RSPTA, 370, 3193
De Pontieu, B., McIntosh, S. W., Carlsson, M., et al. 2007, Sci, 318, 1574
Domínguez Cerdeña, I., Kneer, F., & Sánchez Almeida, J. 2003, ApJL, 582, L55
Dowdy, J. F., Jr., Rabin, D., & Moore, R. L. 1986, SoPh, 105, 35
Dymova, M. V., & Ruderman, M. S. 2005, SoPh, 229, 79
Dymova, M. V., & Ruderman, M. S. 2006, A&A, 459, 241
Edwin, P. M., & Roberts, B. 1982, SoPh, 76, 239
Edwin, P. M., & Roberts, B. 1983, SoPh, 88, 179
Erdélyi, R. 2006, RSPTA, 364, 351
Erdélyi, R., & Fedun, V. 2007, Sci, 318, 1572
Erdélyi, R., & Fedun, V. 2010, SoPh, 263, 63
Erdélyi, R., & Morton, R. J. 2009, A&A, 494, 295
Erdélyi, R., & Taroyan, Y. 2008, A&A, 489, L49
Faurobert, M., Arnaud, J., Vigneau, J., & Frisch, H. 2001, A&A, 378, 627
Fedun, V., Shelyag, S., & Erdélyi, R. 2011a, ApJ, 727, 17
Fedun, V., Shelyag, S., Verth, G., Mathioudakis, M., & Erdélyi, R. 2011b, AnGeo, 29, 1029
Fedun, V., Verth, G., Jess, D. B., & Erdélyi, R. 2011c, ApJL, 740, L46
Goossens, M., Andries, J., & Aschwanden, M. J. 2002, A&A, 394, L39
Goossens, M., Terradas, J., Andries, J., Arregui, I., & Ballester, J. L. 2009, A&A, 503, 213
He, J., Marsch, E., Tu, C., & Tian, H. 2009a, ApJL, 705, L217
He, J.-S., Tu, C.-Y., Marsch, E., et al. 2009b, A&A, 497, 525
Ionson, J. A. 1978, ApJ, 226, 659
Ishikawa, R., Tsuneta, S., Kitakoshi, Y., et al. 2007, A&A, 472, 911
Jess, D. B., Mathioudakis, M., Christian, D. J., et al. 2010, SoPh, 261, 363
Jess, D. B., Mathioudakis, M., Erdélyi, R., et al. 2009, Sci, 323, 1582
Jess, D. B., McAteer, R. T. J., Mathioudakis, M., et al. 2007, A&A, 476, 971
Jess, D. B., Pascoe, D. J., Christian, D. J., et al. 2012a, ApJL, 744, L5
Jess, D. B., Shelyag, S., Mathioudakis, M., et al. 2012b, ApJ, 746, 183
Keys, P. H., Mathioudakis, M., Jess, D. B., et al. 2011, ApJL, 740, L40
Kitiashvili, I. N., Kosovichev, A. G., Mansour, N. N., Lele, S. K., & Wray, A. A. 2012, PhyS, 86, 018403
Kitiashvili, I. N., Kosovichev, A. G., Mansour, N. N., & Wray, A. A. 2011, ApJL, 727, L50
Klimchuk, J. A. 2006, SoPh, 234, 41
Kuridze, D., Morton, R. J., Erdélyi, R., et al. 2012, ApJ, 750, 51
Leenaarts, J., Carlsson, M., & Rouppe van der Voort, L. 2012, ApJ, 749, 136
Leenaarts, J., Rutten, R. J., Carlsson, M., & Uitenbroek, H. 2006, A&A, 452, L15
Luna, M., Terradas, J., Oliver, R., & Ballester, J. L. 2010, ApJ, 716, 1371
Markwardt, C. B. 2009, in ASP Conf. Ser. 411, Astronomical Data Analysis Software and Systems XVIII, ed. D. A. Bohlender, D. Durand, & P. Dowler (San Francisco, CA: ASP), 251

Matsumoto, T., & Kitai, R. 2010, ApJL, 716, L19
Matsumoto, T., & Shibata, K. 2010, ApJ, 710, 1857
Matthaeus, W. H., Zank, G. P., Oughton, S., Mullan, D. J., & Dmitruk, P. 1999, ApJL, 523, L93
McKenzie, J. F., Axford, W. I., & Banaszkiewicz, M. 1997, GeoRL, 24, 2877
Moll, R., Cameron, R. H., & Schüssler, M. 2011, A&A, 533, A126
Moll, R., Cameron, R. H., & Schüssler, M. 2012, A&A, 541, A68
Morton, R., & Erdélyi, R. 2009, A&A, 502, 315
Morton, R. J., Verth, G., Jess, D. B., et al. 2012, NatCo, 3, 1315
November, L. J., & Simon, G. W. 1988, ApJ, 333, 427
Okamoto, T. J., & De Pontieu, B. 2011, ApJL, 736, L24
Orozco Suárez, D., & Bellot Rubio, L. R. 2012, ApJ, 751, 2
Pascoe, D. J., Wright, A. N., & De Moortel, I. 2011, ApJ, 731, 73
Peter, H. 2001, A&A, 374, 1108
Pietarila, A., Hirzberger, J., Zakharov, V., et al. 2009, A&A, 502, 647
Reardon, K. P., Uitenbroek, H., & Cauzzi, G. 2009, A&A, 500, 1239
Rimmele, T. R. 2004, in Proc. SPIE, 5490, 34
Robertson, D., Ruderman, M. S., & Taroyan, Y. 2010, A&A, 515, A33
Ruderman, M. S., & Roberts, B. 2002, ApJ, 577, 475
Ruderman, M. S., Verth, G., & Erdélyi, R. 2008, ApJ, 686, 694
Rutten, R. J. 2006, in ASP Conf. Ser. 354, Solar MHD Theory and Observations: A High Spatial Resolution Perspective, ed. J. Leibacher, R. F. Stein, & H. Uitenbroek (San Francisco, CA: ASP), 276
Rutten, R. J. 2007, in ASP Conf. Ser. 368, The Physics of Chromospheric Plasmas, ed. P. Heinzel, I. Dorotovič, & R. J. Rutten (San Francisco, CA: ASP), 27
Sánchez Almeida, J., Márquez, I., Bonet, J. A., Domínguez Cerdeña, I., & Muller, R. 2004, ApJL, 609, L91
Schrijver, C. J., & Title, A. M. 2003, ApJL, 597, L165
Schuck, P. W. 2006, ApJ, 646, 1358
Shelyag, S., Fedun, V., Erdélyi, R., Keenan, F. P., & Mathioudakis, M. 2012a, in ASP Conf. Ser. 463, The Second ATST-EAST Meeting: Magnetic Fields from the Photosphere to the Corona, ed. T. R. Rimmele, A. Tritschler, & F. e. a. Wöger (San Francisco, CA: ASP), 107
Shelyag, S., Fedun, V., Keenan, F. P., Erdélyi, R., & Mathioudakis, M. 2011a, AnGeo, 29, 883
Shelyag, S., Keys, P., Mathioudakis, M., & Keenan, F. P. 2011b, A&A, 526, A5
Shelyag, S., Mathioudakis, M., & Keenan, F. P. 2012b, ApJL, 753, L22
Soler, R., Oliver, R., & Ballester, J. L. 2009a, ApJ, 699, 1553
Soler, R., Oliver, R., & Ballester, J. L. 2009b, ApJ, 707, 662
Spruit, H. C. 1982, SoPh, 75, 3
Starck, J.-L., & Murtagh, F. 2002, Astronomical Image and Data Analysis (Berlin: Springer)
Stein, R. F., & Nordlund, A. 1998, ApJ, 449, 914
Terradas, J., Goossens, M., & Verth, G. 2010, A&A, 524, A23
Terradas, J., Oliver, R., & Ballester, J. L. 2006, ApJ, 642, 533
Title, A. M., Tarbell, T. D., Topka, K. P., et al. 1989, ApJ, 336, 475
Tomczyk, S., McIntosh, S. W., Keil, S. L., et al. 2007, Sci, 317, 1192
Tu, C.-Y., & Marsch, E. 1995, SSRv, 73, 1
van Ballegooijen, A. A., Asgari-Targhi, M., Cranmer, S. R., & DeLuca, E. E. 2011, ApJ, 736, 3
Van Doorsselaere, T., Debosscher, A., Andries, J., & Poedts, S. 2004, A&A, 424, 1065
Vargas Domínguez, S., Palacios, J., Balmaceda, L., Cabello, I., & Domingo, V. 2011, MNRAS, 416, 148
Vecchio, A., Cauzzi, G., Reardon, K. P., Janssen, K., & Rimmele, T. 2007, A&A, 461, L1
Verth, G., & Erdélyi, R. 2008, A&A, 486, 1015
Vigeesh, G., Fedun, V., Hasan, S. S., & Erdélyi, R. 2012, ApJ, 755, 18
Vögler, A., Shelyag, S., Schüssler, M., et al. 2005, A&A, 429, 335
Wang, T. 2011, SSRv, 158, 397
Wedemeyer-Böhm, S., Lagg, A., & Nordlund, Å. 2009, SSRv, 144, 317
Wedemeyer-Böhm, S., & Rouppe van der Voort, L. 2009, A&A, 507, L9
Wedemeyer-Böhm, S., Scullion, E., Steiner, O., et al. 2012, Natur, 486, 505
Wöger, F., von der Lühe, O., & Reardon, K. 2008, A&A, 488, 375
Zaqarashvili, T. V., & Erdélyi, R. 2009, SSRv, 149, 355
Zaqarashvili, T. V., Khodachenko, M. L., & Rucker, H. O. 2011, A&A, 529, A82